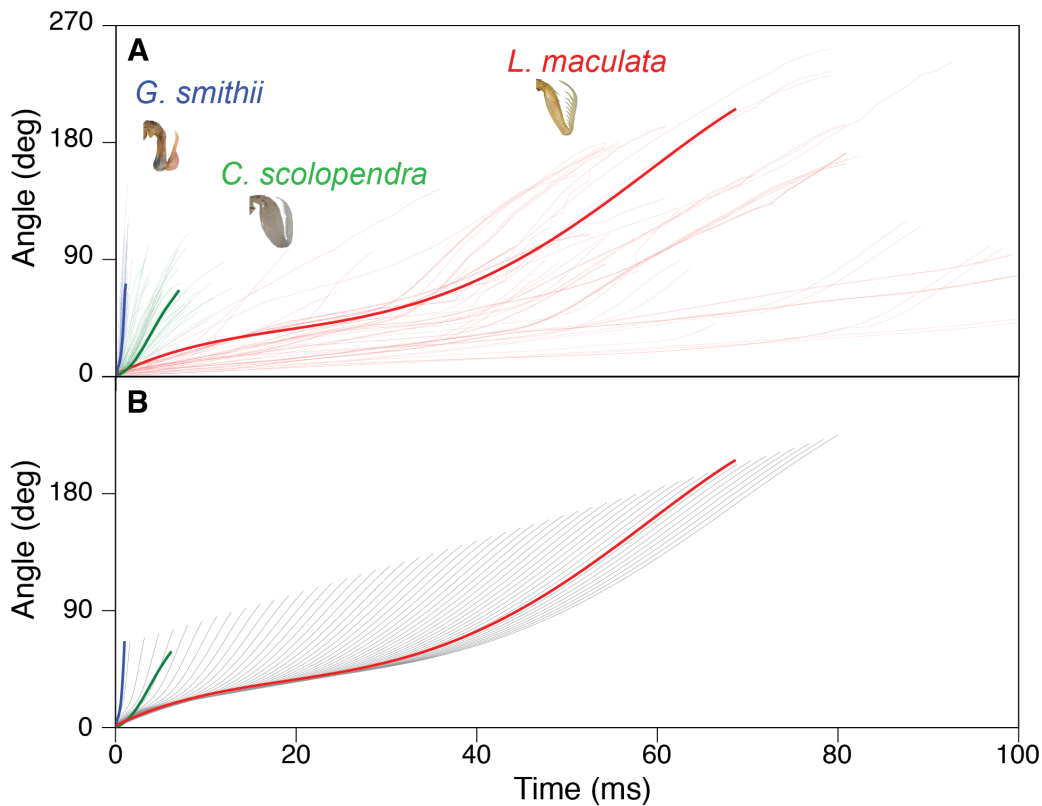# Supplementary Figures

Figure S1. Similar strike kinematics across mantis shrimp permitted generalized strike simulations. (A) Using kinematic data from previous studies and the present study, propodus rotations during raptorial strikes were plotted over time [red: *Lysiosquillina maculata* (deVries, et al. 2012); green: *Coronis scolopendra* (this study); blue: *Gonodactylus smithii* (Cox, et al. 2014)] and the strike that was closest to the mean strike duration for the species was determined for each species (bolded lines). (B) We simulated the kinematics of all species with a fifth-order polynomial for the sigmoidal pattern of one particular strike from *L. maculata*. A sequence of strike simulations is shown (gray curves) that have scaled this strike to varying strike durations to illustrate how this simulated motion compares to the average strikes of each species (i.e., the same strike highlighted in A).
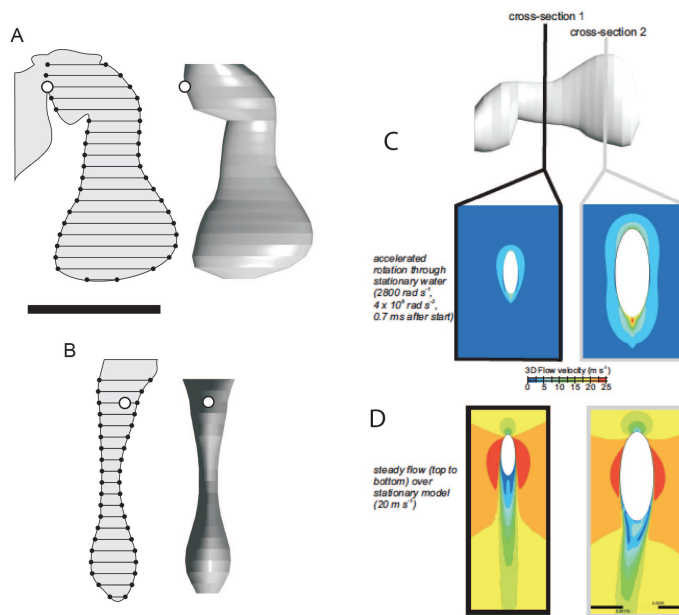
Figure S2. Computational fluid dynamic models and flow patterns in accelerated and steady flow over the model. A. Dimensions of the multi-frustum model fitted to the striking appendage of *Gonodactylus smithii* used in the computational fluid dynamics model. The open circle indicates the center of rotation, and corresponds to the joint location between the carpus and merus (McHenry et al. 2012). The line drawings show the appendage contours (based on Figure 4 from McHenry et al. 2012) together with the axes of the twenty elliptical cylinders that served as base and top planes of the series of frustum segments (final 3D object views on the right). Lateral view images (distal to the toward right of page, dorsal toward the top of the page). **B.** Distal-proximal view images with lateral to the right, dorsal toward the top of the page. Note that the model assumes mirror symmetry about the sagittal plane through the long axis of the appendage. Scale bar, 5 mm. **Flow-patterns in the case of accelerated rotation of the mantis shrimp model (C), and for steady linear flow over the same model (D) as calculated by CFD**. The results for 3D flow velocities are shown on two cross-sectional planes (position indicated in the top image). Note that the perspective differs between the two simulations: the model is moving through stationary water in (C), while the water is moved past the stationary model in (D). This figure shows that the flow pattern in the wake of a short acceleration from rest is notably different from the fully developed wake in a steady translation where two-sided vorticity patterns are present.
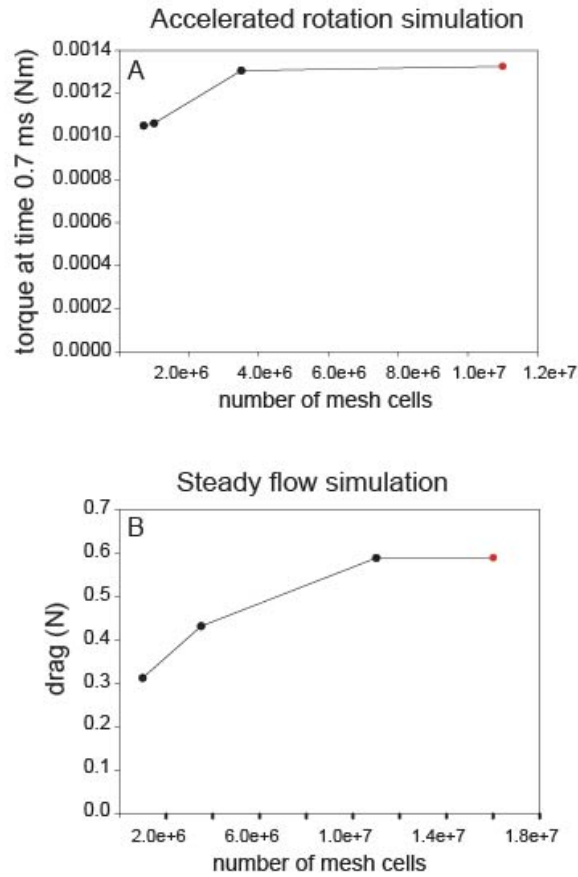
Figure S3. **Results from the mesh convergence analysis showing that the final mesh (red sphere) reached a converged solution for torque on the mantis shrimp model in the simulation of accelerated rotation (A) and for the steady flow simulation of linear flow over the model (B).**

Supplementary Tables

Table S1. Scaling of physical models to achieve the same Reynolds number as calculated for the maximum speed and propodus length of each species (Table 1).

	Maximum speed (m/s)	Propodus length (m)	Scaled appendage (m)	Scale factor	Reynolds Number
G. smithii	30	0.005	0.15	30	1.4×10^5
G. falcatus	30	0.005	0.15	30	1.4×10^5
H. californiensis	3	0.027	0.24	9	7.7×10^4
C. scolopendra	3.4	0.0085	0.23	30	2.7×10^4
L. maculata	3	0.058	0.23	4	1.7×10^5

The scale factors were used for setting the range of flume speeds (Table 3). Given that the maximum flow velocity of the flume is 1 m/s, the scale factor is equivalent to the maximum modeled speed for each scaled-up appendage. *G. falcatus* models were run at speeds based on published values for *G. smithii* (Cox, et al. 2014). *H. californiensis* models were run at speeds based on published values from *L. maculata* (deVries, et al. 2012).

Table S2: Drag (N) on each physical model tested

Flume speed (m/s)		0.038	0.096	0.19	0.28	0.38	0.46	0.55	0.64	0.74	0.83	0.93
	Drag (N)											
G. smithii	open	<0.01	0.02	0.07	0.16	0.24	0.37	0.54	0.74	0.98	1.25	1.58
	closed	<0.01	0.01	0.04	0.09	0.13	0.20	0.30	0.41	0.55	0.69	0.93
G. falcatus	open	<0.01	0.02	0.06	0.12	0.18	0.29	0.43	0.57	0.76	0.96	1.24
	closed	<0.01	<0.01	0.03	0.07	0.10	0.17	0.26	0.36	0.51	0.70	0.78
H. californiensis	open	<0.01	0.03	0.12	0.24	0.38	0.56	0.83	1.12	1.63	2.04	2.63
	closed	<0.01	0.03	0.09	0.18	0.30	0.47	0.69	0.94	1.19	1.45	1.86
C. scolopendra	open	<0.01	0.02	0.06	0.14	0.21	0.33	0.47	0.63	0.84	1.06	1.33
	closed	<0.01	0.02	0.07	0.15	0.24	0.37	0.53	0.70	0.91	1.14	1.53
L. maculata	open	<0.01	0.02	0.05	0.11	0.18	0.29	0.42	0.58	0.74	0.91	0.97
	closed	<0.01	0.02	0.05	0.11	0.17	0.26	0.39	0.51	0.65	0.82	1.02

Each model was tested at a range of flume speeds with the dactyl in the open or closed position. Drag on each model configuration and flume speed is shown here.

Table S3. Hydrodynamic metrics of shape, determined from drag measurements

Species	k Dactyl closed	k Dactyl open	T_d Dactyl closed	T_d Dactyl open	T_d Cylinder
G. smithii (Smasher)	1.06×10^{-1}	5.39×10^{-2}	3.79×10^{-2}	12.0×10^{-2}	8.40×10^{-2}
G. falcatus (Smasher)	1.08×10^{-1}	5.13×10^{-2}	2.08×10^{-2}	3.38×10^{-2}	2.69×10^{-2}
H. californiensis (Undifferentiated)	3.75×10^{-2}	3.08×10^{-2}	1.95×10^{-2}	5.00×10^{-2}	4.87×10^{-2}
C. scolopendra (Spearer)	1.53×10^{-2}	3.95×10^{-2}	1.32×10^{-2}	1.77×10^{-2}	1.62×10^{-2}
L. maculata (Spearer)	3.80×10^{-2}	5.82×10^{-2}	0.95×10^{-2}	0.96×10^{-2}	1.05×10^{-2}

k, shape coefficient; T_d, drag-torque index